Energy &
Environmental
Science

Ferrocene as highly volatile solid additive in non–fullerene organic solar cells with enhanced photovoltaic performance

SCHOLARONE™
Manuscripts

ARTICLE

Ferrocene as highly volatile solid additive in non-fullerene organic solar cells with enhanced photovoltaic performance†

Linglong Ye,‡[a,e] Yunhao Cai,‡*[a] Chao Li,[a] Lei Zhu,[b] Jinqiu Xu,[b] Kangkang Weng,[a] Kangning Zhang,[c] Miaofei Huang,[d] Min Zeng,[e] Tengfei Li,[f] Erjun Zhou,[g] Songting Tan,[e] Xiaotao Hao,[c] Yuanping Yi,[d] Feng Liu,[b] Zhaohui Wang,[h] Xiaowei Zhan[f] and Yanming Sun*[a]

At present, most of the top-performing organic solar cells (OSCs) are processed with high boiling point solvent additives, which usually have a negative effect on the device stability. To overcome this conundrum, we herein introduce a commercially available organic transition metal compound, ferrocene, as a highly volatile solid additive in OSCs. The utilization of ferrocene led to enhanced power conversion efficiency (PCE) and photostability of PM6:Y6 based OSCs in comparison with the devices processed with traditional solvent additive. Systematic analysis revealed that the treatment of ferrocene can effectively increase the molecular crystallinity and thus leads to improved charge transport, which accounts for the achieved higher photovoltaic performance in the corresponding OSCs. Moreover, ferrocene was found to exhibit general applicability in the other five bulk-heterojunction systems. This work not only demonstrates a cost effective and highly volatile solid additive, but also opens a new possibility toward further improvement of PCE and stability of OSCs.

Broader context

The combined efforts in material design, device engineering, morphology control, and theoretical studies have driven the power conversion efficiency (PCE) of organic solar cells (OSCs) to over 17%. Solvent additives such as 1,8-diiodooctane (DIO), and 1-chloronaphthalene (CN) are commonly used to optimize the morphology of the active layers and achieve high performance OSCs. However, the high boiling points of these solvent additives make them difficult to remove in processing and thus lead to an inferior stability of the corresponding devices. Alternatively, we report a commercially available organic transition metal compound ferrocene as a highly volatile solid additive. This novel solid additive was firstly applied in PM6:Y6 system, and a high efficiency of 17.4 % was realized, which is much higher than that of the device without any additive (15.5%) and processed with CN (16.5%). In addition, higher photostability was demonstrated in ferrocene treated devices. More importantly, ferrocene was found to be effective in other five different systems. This work indicates that the application of ferrocene is a cost-effective and useful strategy to obtain efficient and stable OSCs.

Introduction

[a]School of Chemistry, Beihang University, Beijing 100191, P. R. China, E-mail: caiyunhao@buaa.edu.cn; sunym@buaa.edu.cn
[b]School of Chemistry and Chemical Engineering, Shanghai Jiao Tong University, Shanghai 200240, P. R. China
[c]School of Physics State Key Laboratory of Crystal Materials, Shandong University, Jinan 250100, P. R. China
[d]Beijing National Laboratory for Molecular Science, Key Laboratory of Organic Solids, Institute of Chemistry, Chinese Academy of Sciences, Beijing 100190, China
[e]College of Chemistry, Xiangtan University, Xiangtan 411105, P. R. China
[f]Department of Materials Science and Engineering, College of Engineering, Peking University, Beijing 100871, P. R. China
[g]CAS Key Laboratory of Nanosystem and Hierarchical Fabrication, CAS Center for Excellence in Nanoscience, National Center for Nanoscience and Technology, Beijing 100190, P. R. China
[h]Key Laboratory of Organic Optoelectronics and Molecular Engineering, Department of Chemistry, Tsinghua University, Beijing 100084, P. R. China

Organic solar cells (OSCs) offer an appealing choice for harnessing the solar energy due to their distinctive properties including low cost, light weight, mechanical flexibility, etc.[1-3] Currently, the best-performing OSCs exhibited high power conversion efficiency (PCE) of more than 17%.[4-13] The PCE and the long-term stability are thought to be the most pertinent obstacles for the large-scale production of OSCs.[14] For the development of highly efficient and stable OSCs, the optimization of the bulk heterojunction (BHJ) morphology is of vital importance.[15-19]

The use of solvent additives, such as 1,8-diiodooctane (DIO), and 1-chloronaphthalene (CN) is one of the most widely used approaches to optimizing the BHJ morphology.[20-22] These additives have exhibited outstanding effects on promoting the device performance since they can usually adjust the aggregation behavior

of the materials and therefore endow well-defined bicontinuous interpenetrating networks.[23] However, the high boiling point solvent additives are typically difficult to remove sufficiently. The residual solvent additives will undergo a tardiness of drying procedure, which could usually cause an undesirable morphological variation and thus an accelerated performance deterioration.[24,25] In addition, it has been proved that the devices processed with solvent additives are susceptible to photodegradation after exposure to simulated sunlight in ambient conditions.[26,27] Ye et al. also reported that the residual solvent additives can exert a negative effect on the reproducibility of device performance.[28-30] More importantly, some solvent additives are costly, which holds back the widespread application of OSCs.[31-34] In this regard, new insights and methods are in urgent need for the optimization of BHJ morphology of OSCs.

Here, we report a facile approach to boosting the photovoltaic performance and photostability of OSCs by introducing ferrocene into BHJ as a highly volatile solid additive. Ferrocene is a commercial available organic transition metal compound with aromatic nature. Due to its fascinating characters, including low cost, stable, and electrical conductivity, it has many applications in a wide range of scientific areas such as catalyst, sensor, aerospace materials and medical science.[37,38] In the field of OSCs, ferrocene is commonly used as an external or internal potential marker in cyclic voltammetry measurements.[39] Herein, we initially treated PM6:Y6 blend with ferrocene, a high PCE of 17.4% (certified as 16.9%) with an unanticipated short-circuit current density (J_{sc}) of 26.90 mA cm^{-2} was obtained, which is much higher than that of the device without any

additive (15.5%) and with CN solvent additive (16.5%). To the best of our knowledge, the PCE of 17.4% and J_{sc} of 26.90 mA cm^{-2} are among the highest results reported for binary OSCs to date. Insightful characterizations were performed to reveal the function of ferrocene. The increased molecular crystallinity, improved charge transport and suppressed charge recombination achieved in the devices processed with ferrocene are proposed to be the main reasons behind the high performance. Besides, OSCs using ferrocene exhibited better photostability than the CN-processed device. To verify its general applicability, ferrocene was also introduced into five different BHJ systems, which all led to enhanced PCEs.[4,40-48] These results illustrate that ferrocene is a promising volatile solid additive for the fabrication of efficient and stable OSCs. This work also affords an important guideline for further development of OSC in a simple and low cost way.

Results and discussion

Fig. 1 presents the chemical structures of ferrocene, polymer donors and non-fullerene acceptors used in this work. Herein, we mainly took PM6:Y6 system as a representative to investigate the effect of ferrocene on the BHJ morphology. It should be noted here that, except for Fourier transform infrared (FT-IR) spectra and energy dispersive X-ray fluorescence (XRF) spectroscopy measurements, all the samples tested were under post-thermal annealing treatment to achieve the optimum conditions. The ultraviolet–visible (UV-vis) absorptions of ferrocene, PM6, Y6 and their blend processed with
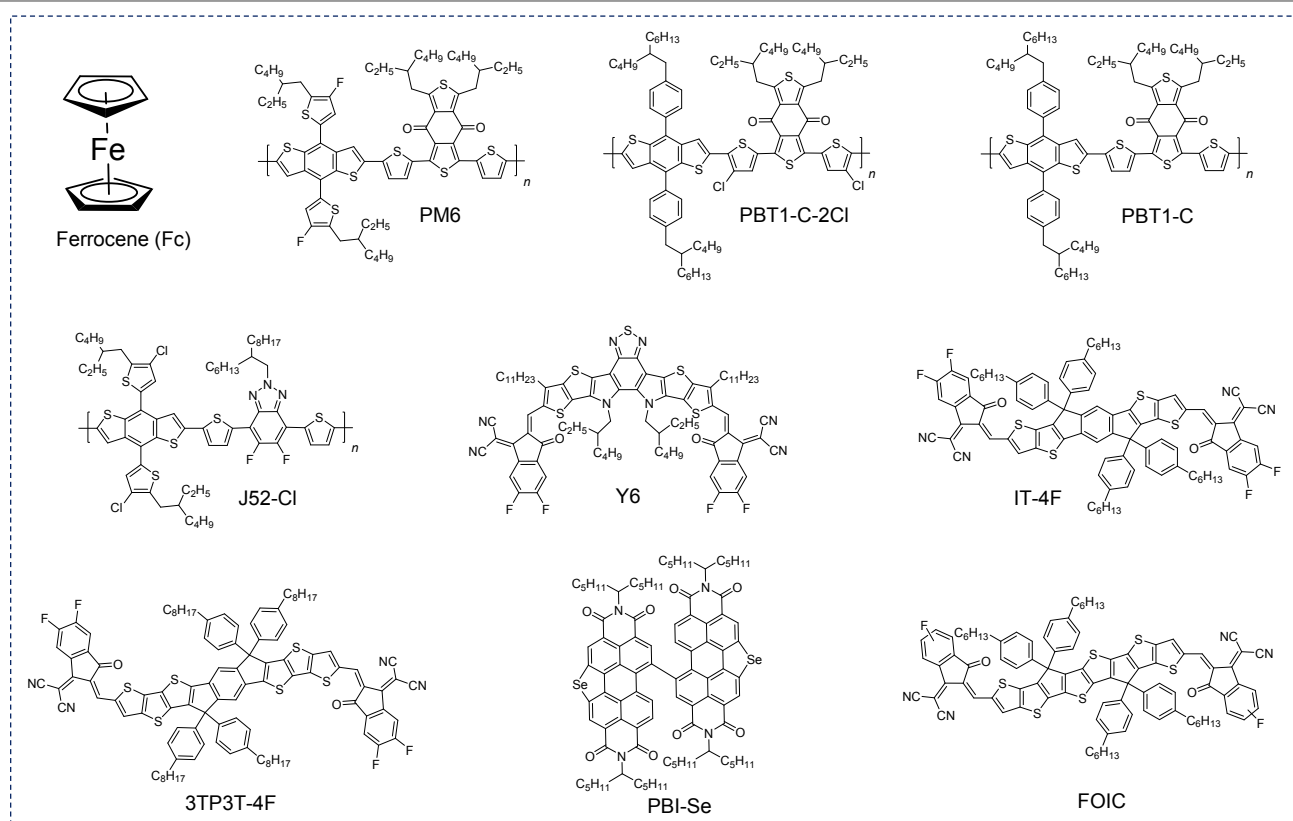

Fig. 1 Chemical structures of ferrocene and photovoltaic materials used in this work.
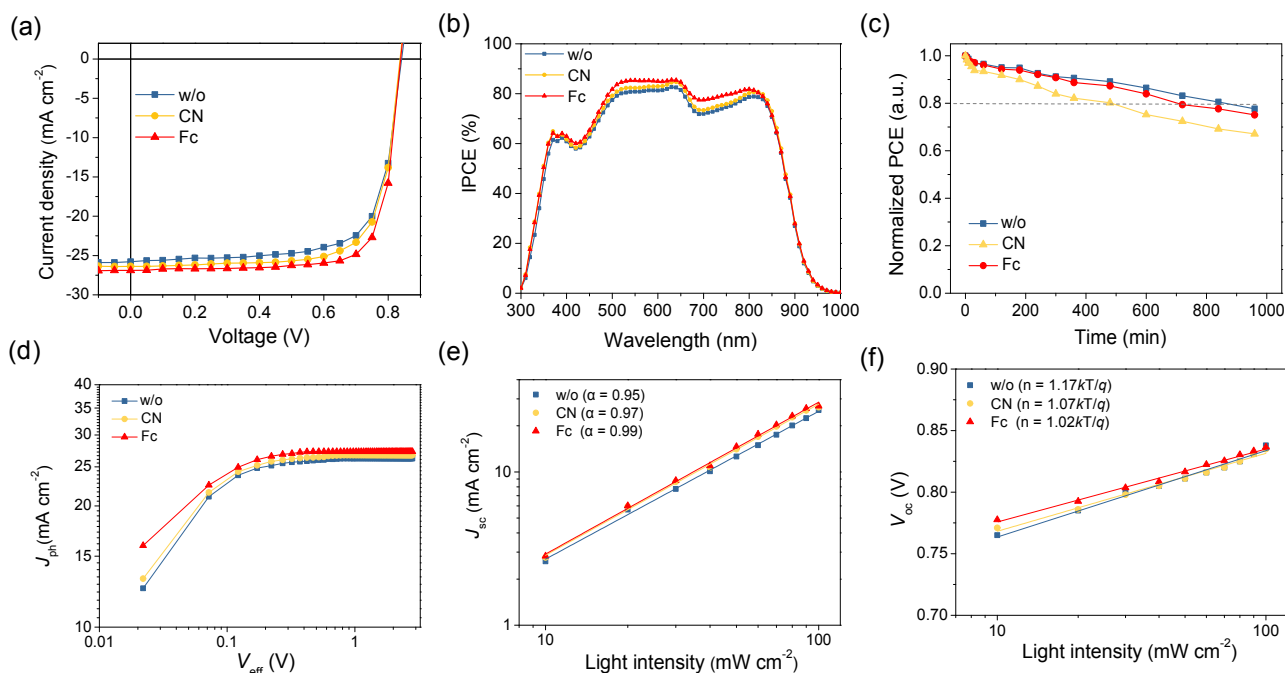
Fig. 2 (a) *J–V* curves of PM6:Y6 devices with different conditions. The corresponding (b) EQE curves, (c) photostability (encapsulated, AM 1.5 radiation to illumination of 100 mW cm⁻²), (d) photocurrent density (J_{ph}) as a function of effective bias (V_{eff}), (e) J_{sc} versus light intensity, and (f) V_{oc} versus light intensity.

different conditions are shown in the Fig. S1 (ESI†). It can be seen that PM6 and Y6 exhibit complementary absorption in a wide absorptions range, and thus a high J_{sc} is expected. The absorption of ferrocene is mainly concentrated in the wavelength range of 380-500 nm. Due to the low molar extinction coefficient (114 M⁻¹ cm⁻¹), it is expected that the addition of a tiny amount of ferrocene into PM6, Y6, and PM6:Y6 blend should have no effect on the absorption spectra. ~~However, the main absorption peaks of PM6, Y6, and PM6:Y6 blend are slightly red-shifted, indicative of enhanced intermolecular π–π stacking in the ferrocene processed films, which will be discussed in the following grazing-incidence wide-angle X-ray scattering (GIWAXS) section.~~

To explore the effect of ferrocene on the photovoltaic performance of OSCs, devices with different processing conditions were fabricated. Representative current density–voltage (*J–V*) characteristics under AM 1.5G illumination (100 mW cm⁻²) are shown in Fig. 2a. Photovoltaic performance of OSC based on PM6:Y6 without any additive was initially evaluated. A moderate PCE of 15.5% with an open-circuit voltage (V_{oc}) of 0.84 V, a J_{sc} of 25.36 mA cm⁻², and a fill factor (FF) of 0.73 was obtained. However, after the addition of ferrocene (6% weight ratio to the blend), the PCE of the device was remarkably improved to 17.4% (certified as 16.9%, Fig. S2, ESI†), accompanied by an extraordinarily high J_{sc} of 26.90 mA cm⁻², a V_{oc} of 0.84 V and a FF of 0.77. As far as we know, this efficiency and J_{sc} are among the highest values reported for OSCs so far. Fig. S3 (ESI†) presents the histogram of the PCE parameter in 40 devices processed with different conditions. To investigate the impact of different amounts of ferrocene on the performance of PM6:Y6 based OSCs, we changed the weight ratio of ferrocene to the blends from 5% to 8%. And high PCEs over 16.5% could be still obtained with varied amounts of ferrocene. The corresponding results are summarized in the supporting information (Fig. S4 and Table S1,

ESI†). Table S2 (ESI†) and Table S3 (ESI†) summarize the photovoltaic parameters of CN and ferrocene processed PM6:Y6 devices with different thermal annealing time. Representative current density–voltage (*J–V*) characteristics under AM 1.5G illumination (100 mW cm⁻²) are shown in Fig. S5 and Fig. S6 (ESI†). Besides, OSCs processed with traditional solvent additive CN were also prepared for comparison, which is typically used as the solvent additive for PM6:Y6 binary OSCs.[4] Consequentially, the device adopting CN as the solvent additive produced a maximum PCE of 16.5%, with a V_{oc} of 0.84 V, a J_{sc} of 26.21 mA cm⁻², and a FF of 0.75.

In order to verify its general applicability in OSCs, ferrocene was further applied into OSCs based on different material combinations, including PM6:3TP3T-4F, PBT1-C-2Cl:IT-4F, PM6:PBI-Se, PBT1-C:FOIC, and J52-2Cl:IT-4F. Encouragingly, ferrocene has served as a successful additive in all these systems. Better performance, especially higher J_{sc}s, was achieved in ferrocene treated OSCs than those of devices without additive and even with solvent additives. The detailed photovoltaic parameters are summarized in Table 1. It is worth noting that ferrocene can effectively improve J_{sc} without sacrificing the V_{oc} of the corresponding devices. In comparison with OSCs processed with conventional solvent additives, higher V_{oc}s were obtained in devices using ferrocene as a solid additive, which are even comparable to the device without any additive. The external quantum efficiency (EQE) spectra of OSCs processed with different conditions are displayed in Fig. 2b and Fig. S7 (ESI†). It can be seen that the introduction of ferrocene in these systems mainly led to higher EQE values in the region of 400–800 nm, contributing to the enhancement in J_{sc}s. The calculated J_{sc}s are in good agreement with the values achieved from the *J–V* measurements within 4% mismatch.

Additionally, we compared the stability of the optimal PM6:Y6 OSCs processed without any additive, with CN and ferrocene under

Table 1. Summary of photovoltaic parameters of OSC systems in this study.

Active layer	additive	V_{oc}(V)	J_{sc}(mA cm^{-2})	FF	PCE[a](%)
PM6:Y6	w/o	0.838±0.002	25.12±0.22	0.72±0.01	15.55 (15.16)
	0.5% CN	0.837±0.004	25.90±0.31	0.74±0.01	16.50 (16.04)
	ferrocene[b]	0.838±0.002	26.71±0.20	0.76±0.01	17.40 (17.01)
PM6:3TP3T-4F	w/o	0.927±0.002	18.56±0.21	0.72±0.02	12.92 (12.39)
	0.5% CN	0.919±0.004	19.86±0.30	0.73±0.02	13.91 (13.32)
	ferrocene	0.928±0.003	19.90±0.30	0.75±0.01	14.27 (13.86)
PBT1-C-2Cl:IT-4F	w/o	0.868±0.002	17.02±0.20	0.69±0.01	10.55 (10.19)
	0.25% DIO	0.839±0.003	19.01±0.24	0.74±0.02	12.22 (11.80)
	ferrocene	0.868±0.002	19.21±0.35	0.72±0.02	12.59 (12.01)
PM6:PBI-Se	w/o	1.007±0.005	11.33±0.21	0.64±0.01	7.57 (7.30)
	0.5% DIO	1.002±0.004	11.52±0.34	0.67±0.02	8.27 (7.73)
	ferrocene	1.007±0.003	12.22±0.23	0.66±0.02	8.55 (8.12)
PBT1-C:FOIC	w/o	0.805±0.004	19.88±0.36	0.61±0.01	10.16 (9.76)
	0.5% CN	0.787±0.003	23.08±0.39	0.62±0.01	11.68 (11.26)
	ferrocene	0.804±0.002	23.70±0.19	0.61±0.01	11.86 (11.62)
J52-Cl:IT-4F	w/o	0.835±0.005	18.83±0.25	0.65±0.02	10.73 (10.22)
	0.25% DIO	0.800±0.003	20.25±0.27	0.72±0.02	12.15 (11.67)
	ferrocene	0.836±0.004	20.39±0.33	0.69±0.01	12.18 (11.76)

[a] Average values with standard deviation were obtained from 10 devices.
[b] The amounts of ferrocene added in the different systems are summarized in the supporting information.

continuous illumination for 960 min. The details of the photostability test can be found in the experimental section. As shown in Fig. 2c, the device without any additive demonstrated the best photostability. However, the device treated with ferrocene exhibited evidently superior photostability than that of CN processed device. In details, 20% PCE loss occurred around 840, 480 and 720 min for the control, CN and ferrocene processed devices, respectively. The better photostability achieved in ferrocene processed device demonstrates the great potential of this novel solid additive for the fabrication of highly stable OSCs.

To probe the origin of the improved J_{sc} and FF, the saturation current density (J_{sat}) and charge dissociation probability (P(E,T)) of the optimal devices fabricated with different conditions were measured. The photocurrent density (J_{ph}) versus the effective voltage (V_{eff}) curves of the devices are depicted in Fig. 2d. J_{ph} is denoted as the gap between J_L and J_D, in which J_L and J_D represents the current density under illumination and in the dark, respectively. V_{eff} is defined as difference between V_0 and V_a, where V_0 is the voltage at which J_{ph} is zero and V_a is the applied bias voltage.[49] It was found that J_{ph} reached J_{sat} when V_{eff} approached 2 V, implying that all the excitons inside the devices were dissociated into free charge carriers

and collected by the electrodes. J_{sat}s of devices without any additive, using CN and ferrocene additives were 26.26, 26.72 and 27.31 mA cm^{-2}, respectively. The improved J_{sat} value in ferrocene processed device confirmed that ferrocene actually assisted the photoharvesting of PM6:Y6 blend. Under the short-circuit condition, the calculated P(E,T) values for these devices were 95.8%, 96.9% and 97.7%, respectively. The results demonstrate that the introduction of ferrocene facilitated charge extraction and yielded higher J_{sc} and FF.

The dependence of J_{sc} and V_{oc} on light intensity (P_{light}) was conducted to reveal the influence of ferrocene on the charge recombination of the corresponding device. The power-law equation $J_{sc} \propto (P_{light})^\alpha$ expresses the relationship of J_{sc} and P_{light}, in which α represents the extent of bimolecular recombination behavior.[50] As displayed in Fig. 2e, the extracted α values for devices without and with CN additive were 0.95 and 0.97, respectively, while for device processed with ferrocene additive, α was 0.99, indicating that bimolecular recombination was effectively suppressed in the ferrocene processed device under short circuit condition. The measurement of the V_{oc} as a function of P_{light} helps study the trap-assisted recombination inside the devices. By calculating the slope of the V_{oc} versus the natural logarithm of the P_{light}, the corresponding

mechanism of recombination can be clarified (Fig. 2f).[51] Generally, under open-circuit condition, if the mechanism is dominated by bimolecular recombination, a slope of kT/q is expected, where k is the Boltzmann constant, T is Kelvin temperature, and q is the elementary charge. Alternatively, when a signature of monomolecular or trap-assisted recombination is involved, higher dependence of the V_{oc} on the light intensity with a slope of $2kT/q$ will be observed. In this work, OSCs without additive and with CN solvent additive showed slopes of $1.17kT/q$ and $1.07kT/q$, respectively. When using ferrocene as a solid additive, the slope was $1.02kT/q$. Such results revealed that the utilization of ferrocene can effectively suppress trap-assisted recombination of the OSCs and therefore contributes to the better performance.

GIWAXS was performed to investigate the molecular packing and orientation of neat and blend films.[52,53] The 2D GIWAXS diffraction patterns and the corresponding line-cut profiles of the neat films of PM6 and Y6 are shown in Fig. S8 and Fig. S9 (ESI†). PM6 and Y6 films both showed strong (010) diffraction peaks at $q_z = 1.68$ Å^{-1} and 1.77 Å^{-1}, in the out-of-plane (OOP) direction, corresponding to the π-π stacking distances of 3.74 Å and 3.56 Å, respectively. This suggests that PM6 and Y6 both adopted a preferred face-on orientation of molecule ordering in the neat films. Notably, it can be seen that the treatment of ferrocene did not strongly influence the lamellar stacking and π-π stacking of PM6. But for Y6, the intensities of the lamellar and π-π stacking peaks increased largely both in in-plane (IP) and OOP directions for ferrocene processed film, indicating that the processing of ferrocene could endow Y6 film with a more orderly structure. Such observation also conveys that the treatment of ferrocene mainly affects the packing of Y6 acceptor. GIWAXS patterns of PM6:Y6 blend films with different processing conditions are illustrated in Fig. 3. The blend film without additive also adopted
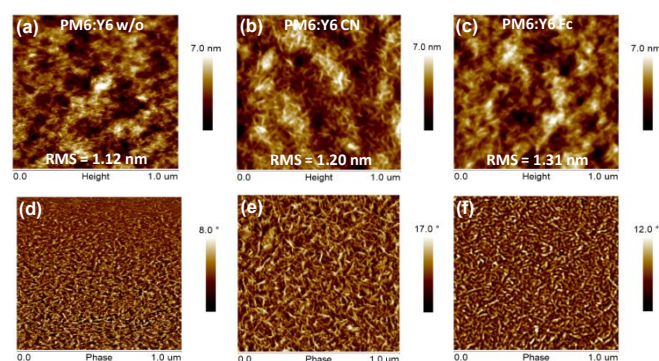

Fig. 4 (a-c) AFM height and (d-f) phase images of PM6:Y6 blend films under different processing methods.

a predominantly face-on orientation, evidenced by the strong lamellar stacking peak (100) in IP direction and the obvious π-π stacking peak (010) in OOP direction. When the blend film was treated by ferrocene, the face-on orientation still maintained, which is favorable of the vertical charge transport. In addition, more pronounced π–π reflection peak and lamellar peak were observed, demonstrating more ordered molecular stacking and higher crystallinity of the BHJ film. GIWAXS data for the blend films processed with CN were also collected for comparison, the optimum CN-processed thin film displayed moderate lamellar and π-π stacking in GIWAXS. The full width at half-maximum (FWHM) of the out-of-plane (010) diffraction peaks and the corresponding crystal coherence lengths (CCLs) for the neat and blend films under different conditions are summarized in Table S4 (ESI†). The results manifest that the significantly increased crystallinity caused by the addition of
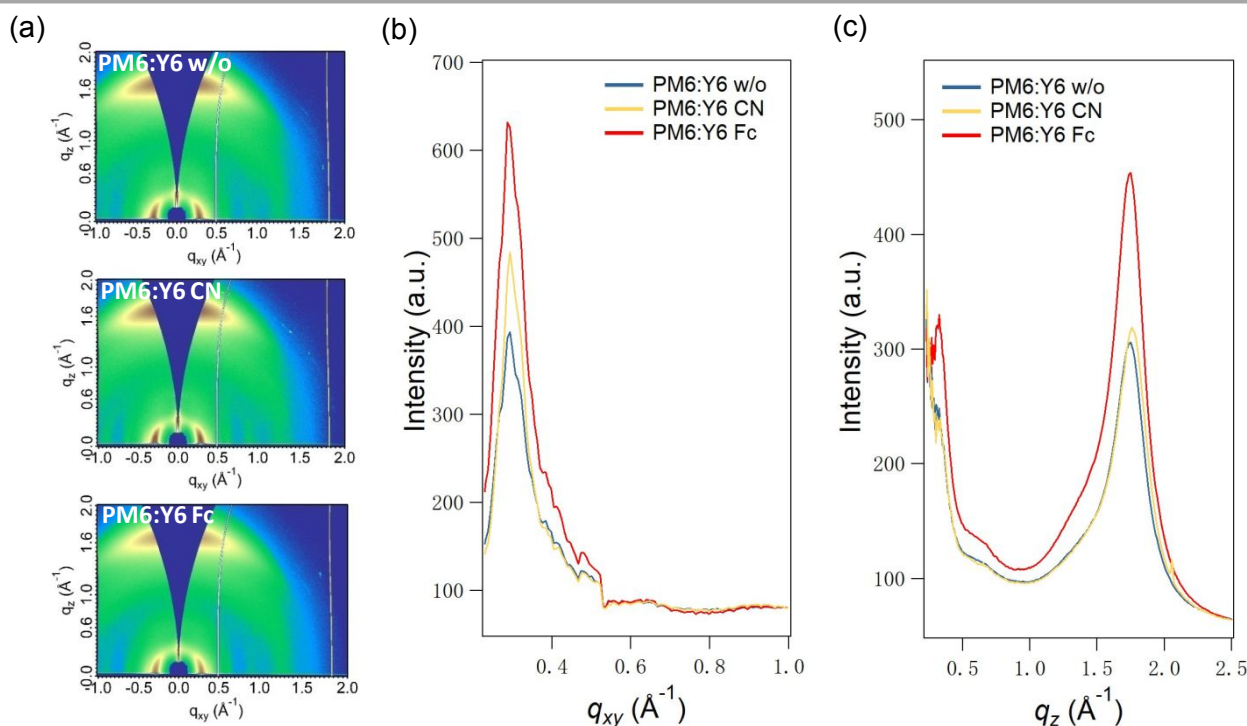

Fig. 3 2D GIWAXS patterns for (a) PM6:Y6 with different conditions (b) IP and (c) OOP line-cut profiles of GIWAXS images with corresponding conditions.
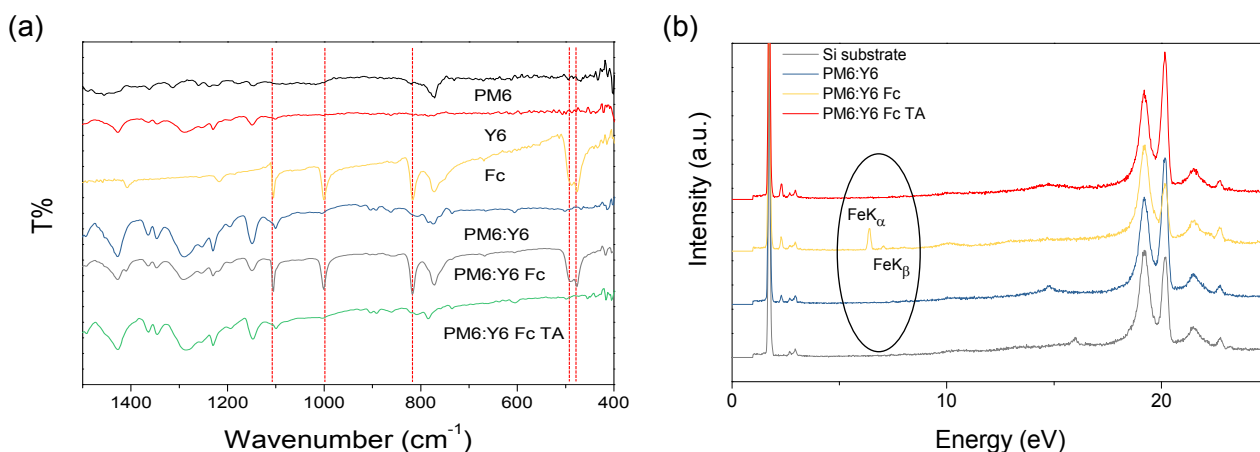
Fig. 5 (a) FT-IR spectra and (b) energy dispersive XRF spectra of PM6:Y6 blend films with different conditions.

ferrocene into the blend should be a major reason for the improved photovoltaic performance achieved in ferrocene processed OSCs.

Subsequently, the tapping mode atomic force microscopy (AFM) was adopted to provide the topography information of the films. As shown in Fig. 4, the blend films processed with different conditions all showed similar smooth and uniform surface morphology. Obvious fiber distribution was clearly seen in these films, which has previously been proved to be beneficial to the exciton dissociation and charge transportation in OSCs.[54-56] In details, the as-cast PM6:Y6 blend film showed a root mean square (RMS) value of 1.12 nm. The BHJ blend using CN additive showed a RMS of 1.20 nm. The blend film processed with ferrocene exhibited comparatively larger fibril width and phase separation with a higher RMS of 1.31 nm. We also treated pristine PM6 and Y6 films with ferrocene to investigate the effect of ferrocene. With the treatment of ferrocene, the RMS of neat PM6 film showed a slightly improvement from 1.70 to 2.07 nm, and that of Y6 film was dramatically enhanced from 1.80 to 7.30 nm (Fig. S10, ESI†). This observation suggests that the use of ferrocene could lead to better phase separation of active layer and more condensed molecular arrangement, consistent well with the GIWAXS results. To study the evolution of the morphology, we collected AFM micrographs with increasing ageing time (Fig. S11, ESI†). It was found that with the illumination time increases, the molecule aggregation becomes stronger, which could result in unfavorable phase separation and oversized domains. Besides, ordered structure with well-defined fibrillar structure was observed before illumination. The formed fibril network could optimize phase separation scale and ensure efficient exciton dissociation and charge carrier transport. However, with the increase of light illumination time, the fibril nanostructure becomes more obscure, which also contributes to the degenerated morphology.

The charge carrier mobilities of the blend films under different conditions were evaluated by space charge limited current (SCLC) method (Fig. S12, ESI†). The configuration of ITO/PEDOT:PSS/active layer/MoO$_3$/Al and ITO/ZnO/active layer/PFN-Br/Al were employed to measure the hole mobility and electron mobility respectively. The calculated hole mobility and electron mobility of the devices without any additive were 3.62× 10^{-4} cm^2 V^{-1} s^{-1} and 4.56× 10^{-4} cm^2 V^{-1} s^{-1},

while for device processed with CN, the hole mobility and electron mobility were 5.20× 10^{-4} cm^2 V^{-1} s^{-1} and 5.77× 10^{-4} cm^2 V^{-1} s^{-1}, respectively. Upon the treatment of ferrocene, the hole mobility was increased to 6.31× 10^{-4} cm^2 V^{-1} s^{-1}, and the electron mobility was improved to 7.13× 10^{-4} cm^2 V^{-1} s^{-1}. The enhanced charge mobility accounts for the higher J_{sc} and FF achieved in ferrocene processed devices, which also agrees well with the aforementioned GIWAXS results.

The steady-state photoluminescence (PL) and time-resolved photoluminescence (TRPL) measurement were carried out to gain a deeper insight into the charge transfer efficiency of the blends under different conditions. After blending the donor and acceptor, obvious PL quenching was observed for both blend without additive and ferrocene treated blend, indicative of the efficient exciton dissociation in the devices (Fig. S13, ESI†). As shown in Fig. S14 (ESI†), the PM6 pristine film showed an emission spectrum at 700 nm with an average exciton lifetime (τ) of 288 ps, while the pure Y6 film presented a τ of 421 ps at 900 nm. After blending the two materials, the τ was significantly decreased to 37 ps at 700 nm, and 57 ps at 900 nm, implying efficient charge transfer took place in this blend. More efficient charge transfer was verified from a shorter lifetime of 35 ps at 700 nm, and 53 ps at 900 nm in the ferrocene processed thin film. The better charge transfer occurred in OSC using ferrocene as a solid additive is expected to play a considerable role in improving the device performance.

In view of a combination of characterization discussed above, we speculate the working mechanism of ferrocene in OSC as follows. The addition of ferrocene into the active layer occupies some space. During the thermal annealing procedure, the ferrocene is volatilizing continuously, leaving PM6 and Y6 more room to aggregate and thus form more compact and ordered molecular structures. We collected the AFM images of the ferrocene processed blend films with different thermal annealing time (Fig. S15, ESI†). It was found that with the increase of thermal annealing time, the root-mean-square (RMS) value increases in sequence (from 0.77 to 0.90 nm), indicative of enhanced molecular aggregation during the thermal annealing process. To verify the working mechanism we proposed, we carried out the thermogravimetric analysis (TGA) first. The sample is the blend of PM6, Y6 and ferrocene, and the heating rate is 10 °C min^{-1}.

Considering that the volatilization of ferrocene may slower in the blend, we hold the heating temperature at 100 °C for 15 min. As shown in Fig. S16 (ESI†), there is a clear weight loss at 100 °C. It is known that the polymer donor PM6 and acceptor Y6 has T_d (5% weight loss) over 300 °C.[4,57] Accordingly, we believe the weight loss at 100 °C indicates that the solid additive ferrocene volatizes at 100 °C, and ferrocene volatilized completely within 15 min.

Moreover, theoretical calculation was performed to further investigate the molecular interaction of ferrocene/PM6 and ferrocene/Y6 using density functional theory (DFT) (Fig. S17, ESI†).[58] The calculated results show that the binding energies of ferrocene with PM6 and Y6 are generally negative and the strongest ones are similar. It seems that the PM6 and Y6 molecules can be can be bridged by the ferrocene, which increases the molecular interactions between PM6 and Y6 molecules. It is worth noting that the binding energies of ferrocene with PM6 and Y6 are moderate. Therefore, ferrocene can be evaporated easily. When ferrocene volatilized completely, the intensities of the lamellar and π-π stacking peaks of Y6 molecules in the blend was found to increase largely both in in-plane and out-of-plane directions, indicating that the processing of ferrocene could endow Y6 film with a more orderly structure. Based on a series of characterizations and experimental results, we propose that during the thermal annealing procedure, the ferrocene is volatilizing continuously, leaving PM6 and Y6 more room to aggregate and thus form more compact and ordered molecular structures. Y6 is much more likely to crystallize than PM6 during the thermal annealing process, agreeing well with the GIWAXS data.

Since the remaining ferrocene may become a trap for efficient charge transport, the certification of the volatilization of ferrocene in the blend is necessary. The ferrocene was firstly spin cast onto ITO and silicon substrates and then heated at 100 °C. We observed that ferrocene can completely volatilize within 70 s (Fig. S18, ESI†). In addition, FT-IR spectra and XRF spectroscopy were used to offer a more solid proof of the existence of ferrocene in the active layer. From the FT-IR spectra (Fig. 5a), we found that ferrocene exhibited characteristic peaks at 1105 cm^{-1}, 1000 cm^{-1}, 816 cm^{-1}, 488 cm^{-1} and 476 cm^{-1}. When it was added into PM6:Y6 blend, the peaks assigned to ferrocene were still clearly seen. As expected, these peaks were disappeared after thermal annealing, indicative of that the solid additive was completely volatilized. On the other hand, XRF spectroscopy is a standard technique for elemental analysis using ionization of atoms and energy dispersive spectroscopy of emitted high energy photon (X-rays). The emitted photons are features of specific atomic orbital transitions. We used the strategy of tracing the emitted XRF signals of iron atom to determine whether there is residual ferrocene. Fig. 5b displays the XRF spectra of PM6:Y6 blend treated with different conditions. Iron K$_\alpha$ and K$_\beta$ peaks from PM6:Y6 blend with ferrocene were located at 6.40 and 7.06 keV. After thermal annealing, the fluorescence signals of iron atom were disappeared. These observations add further credence to the hypothesis that the ferrocene in the blend is completely removed by heating process.

Conclusions

In conclusion, ferrocene, a commercial available organic transition metal compound was successfully applied into OSCs as a solid additive. Compared to traditional solvent additives, ferrocene possesses lower price and better stability, these features make it a desirable candidate for the large-scale fabrication of OSCs. Comprehensive investigations have been performed to study the effect of ferrocene on photovoltaic performance of OSCs. Ferrocene was found to play a vital role by bringing multiple advantageous effects including increasing molecular crystallinity, promoting charge mobility and suppressing charge recombination. As a result, after the introduction of ferrocene, PM6:Y6 devices yielded a high efficiency of 17.4%, which is much higher than those of the control device (15.5%) and device processed with CN (16.5%). We also showed that ferrocene treatment can be effective in different BHJ systems, revealing its general applicability in OSCs. Moreover, we demonstrated that ferrocene can be completely removed from blend via thermal annealing procedure, thus giving rise to a superior stability of ferrocene processed devices. Our work suggests that the utilization of ferrocene as a highly volatile solid additive is a cost-effective yet useful approach toward the fabrication of highly efficient and stable OSCs.

Author contributions

L.Y., Y.C. and Y.S. conceived the project; Y.S. directed the project; L.Y. and Y.C. fabricated and characterized the devices; L.Z., J.X. and F.L. performed the morphology characterization; K.K. performed AFM measurements; K.Z. and X.H. performed TRPL measurements; M.Z. performed SCLC measurements; M.H. and Y.Y. performed the DFT calculations; C.L.,T.L., E.Z., S.T.,Z.W. and X.Z. developed the donor and acceptor materials; L.Y., Y.C. and Y.S. wrote the manuscript; All authors commented on the manuscript.

Conflicts of interest

There are no conflicts to declare.

Acknowledgements

References

1   D. Hu, Q. Yang, H. Chen, F. Wobben, V. M. Le Corre, R. Singh, T. Liu, R. Ma, H. Tang, L. J. A. Koster, T. Duan, He. Yan, Z. Kan, Z. Xiao and S. Lu, *Energy Environ. Sci.*, 2020, **13**, 2134-2141.

2   A. Polman, M. Knight, E. C. Garnett, B. Ehrler and W. C. Sinke, *Science,* 2016, **352**, aad4424.

3   L. Meng, Y. Zhang, X. Wan, C. Li, X. Zhang, Y. Wang, X. Ke, Z. Xiao, L. Ding, R. Xia, H.-L.Yip, Y. Cao, Y. Chen, *Science*, 2018, **361**, 1094-1098.

4   J. Yuan, Y. Zhang, L. Zhou, G. Zhang, H.-L. Yip, T.-K. Lau, X. Lu, C. Zhu, H. Peng, P. A. Johnson, M. Leclerc, Y. Cao, J. Ulanski, Y. Li and Y. Zou, *Joule,* 2019, **3**, 1140-1151.

5   Y. Cui, H. Yao, J. Zhang, T. Zhang, Y. Wang, L. Hong, K. Xian, B. Xu, S. Zhang, J. Peng, Z. Wei, F. Gao and J. Hou, *Nat. Commun.,* 2019, **10**, 2515.

6   L. Zhan, S. Li, T.-K. Lau, Y. Cui, X. Lu, M. Shi, C.-Z. Li, H. Li, J. Hou and H. Chen, *Energy Environ. Sci.*, 2020, **13**, 635-645.

7   Y. Lin, B. Adilbekova, Y. Firdaus, E. Yengel, H. Faber, M. Sajjad, X. Zheng, E. Yarali, A. Seitkhan, O. M. Bakr, A. El-Labban, U. Schwingenschlogl, V. Tung, I. McCulloch, F. Laquai and T. D. Anthopoulos, *Adv. Mater.*, 2019, **31**, 1902965.

8   C. Sun, S. Qin, R. Wang, S. Chen, F. Pan, B. Qiu, Z. Shang, L. Meng, C. Zhang, M. Xiao, C. Yang and Y. Li, *J. Am. Chem. Soc.*, 2020, **142**, 1465-1474.

9   J. Song, C. Li, L. Zhu, J. Guo, J. Xu, X. Zhang, K. Weng, K. Zhang, J. Min, X. Hao, Y. Zhang, F. Liu and Y. Sun, *Adv. Mater.*, 2019, **31**, 1905645.

10   Y. Sun, M. Chang, L. Meng, X. Wan, H. Gao, Y. Zhang, K. Zhao, Z. Sun, C. Li, S. Liu, H. Wang, J. Liang and Y. Chen, *Nat. Electron.*, 2019, **2**, 513-520.

11   Q. Liu, Y. Jiang, K. Jin, J. Qin, J. Xu, W. Li, J. Xiong, J. Liu, Z. Xiao, K. Sun, S. Yang, X. Zhang and L. Ding, *Sci. Bull.*, 2020, **65**, 272-275.

12   B. Fan, M. Li, D. Zhang, W. Zhong, L. Ying, Z. Zeng, K. An, Z. Huang, L. Shi, G. C. Bazan, F. Huang and Y. Cao, *ACS Energy Lett.*, 2020, **5**, 2087-2094.

13   T. Wang, R. Sun, M. Shi, F. Pan, Z. Hu, F. Huang, Y. Li and J. Min, *Adv. Energy Mater.*, 2020, **10**, 2000590

14   W. R. Mateker and M. D. McGehee, *Adv. Mater.*, 2017, **29**, 1603940.

15   X. Li, G. Huang, W. Chen, H. Jiang, S. Qiao, and R. Yang ACS *Appl. Mater. Interfaces* 2020, **12**, 16670–16678.

16   Y. Kim, S. A. Choulis, J. Nelson, D. D. C. Bradley, S. Cook and J. R. Durant, *Appl. Phys. Lett.*, 2005, **86**, 063502.

17   G. Li, V. Shrotriya, J. Huang, Y. Yao, T. Moriarty, K. Emery and Y. Yang, *Nat. Mater.* 2005, **4**, 864-868.

18   K. Weng, L. Ye, L. Zhu, J. Xu, J. Zhou, X. Feng, G. Lu, S. Tan, F. Liu and Y. Sun, *Nat. Commun.*, 2020, **11**, 2855.

19   Y. Xie, Y. Cai, L. Zhu, R. Xia, L. Ye, X. Feng, H.-L. Yip, F. Liu, G. Lu, S. Tan and Y. Sun, *Adv. Funct. Mater.*, 2020, **30**, 2002181.

20   Z. He, B. Xiao, F. Liu, H. Wu, Y. Yang, S. Xiao, C. Wang, T. P. Russell and Y. Cao, *Nat. Photon.*, 2015, **9**, 174-179.

21   J. K. Lee, W. Ma, C. J Brabec, J. Yuen, Moon, S. J, J. Y. Kim, K. Lee, G. C. Bazan and A. J. Heeger, *J. Am. Chem. Soc.*, 2008, **130**, 3619-3623.

22   C. Mcdowell, M. Abdelsamie, M. F. Toney and C. G. Bazan, *Adv. Mater.*, 2018, **30**,1707114.

23   F. Machui, P. Maisch, I. Burgués-Ceballos, S. Langner, J. Krantz, T. Ameri and C. J. Brabec, *ChemPhysChem.*, 2015, **16**, 1275-1280.

24   W. Z. Cai, P. Liu, Y. C. Jin, Q. F. Xue, F. Liu, T. P. Russell, F. Huang, H. L. Yip and Y. Cao, *Adv. Sci.*, 2015, **2**, 1500095.

25   H. Li, D. He, P. Mao, Y. Wei, L. Ding and J. Wang, *Adv. Energy Mater.*, 2017, **7**, 1602663

26   B. J. T. Villers, K. A. O'Hara, D. P. Ostrowski, P. H. Biddle, S. E. Shaheen, M. L. Chabinyc, D. C. Olson and N. Kopidakis, *Chem. Mater.*, 2016, **28**, 876-884.

27   D. H. Wang, A. Pron, M. Leclerc and A. J. Heeger, *Adv. Funct. Mater.*, 2013, **23**, 1297.

28   L. Ye, Y. Jing, X. Guo, H. Sun, S. Zhang, M. Zhang, L. Huo and J. Hou, *J. Phys. Chem. C*, 2013, **117**, 14920–14928.

29   C. McDowell, M. Abdelsamie, M. F. Toney and G. C. Bazan, *Adv. Mater.*, 2018, **30**, 1707114.

30   A. Classen, T. Heumueller, I. Wabra, J. Gerner, L. Y. K. He, N. Einsiedler, N. Li, G. J. Matt, A. Osvet, X. Y. Du, A. Hirsch and C. J. Brabec, *Adv. Energy Mater.*, 2019, **9**, 1902124.

31   R. Yu, H. Yao, L. Hong, Y. Qin, J. Zhu, Y. Cui, S. Li and J. Hou, *Nat. Commun.*, 2018, **9**, 4645

32   L. Liu, Y. Kan, K. Gao, J. Wang, M. Zhao, H. Chen, C. Zhao, T. Jiu, A. K. Y. Jen and Y. Li, *Adv. Mater.*, 2020, **32**, 1907604.

33   J. Fu, S. Chen, K. Yang, S. Jung, J. Lv, L. Lan, H. Chen, D. Hu, Q. Yang, T. Duan, Z. Kan, C. Yang, K. Sun, S. Lu, Z. Xiao and Y. Li, *iScience*, 2020, **23**, 100965.

34   J. Zhao, Y. Li, G. Yang, K. Jiang, H. Lin, H. Ade, W. Ma and H. Yan, *Nat. Energy,* 2016, **1**, 15027-15040.

35   K. H. Park, Y. An, S. Jung, H. Park and C. Yang, *Energy Environ. Sci.*, 2016, **9**, 3464-3471.

36   V. Turkovic, S. Engmann, N. Tsierkezos, H. Hoppe, U. Ritter and G. Gobsch, *ACS Appl. Mater. Interfaces*, 2014, **6**, 18525-18537.

37   D. R. van Staveren and N. Metzler-Nolte, *Chem. Rev.*, 2004, **104**, 5931-5986.

38   M. F. R. Fouda, M. M. Abd-Elzaher, R. A. Abdelsamaia and A. A. Labib, *Appl. Organometal. Chem.*, 2007, **21**, 613-625.

39   R. R. Gagne, C. A. Koval and G. C. Lisensky, *Inorg. Chem.*, 1980, **19**, 2854-2855.

40   Q. Fan, Y. Wang, M. Zhang, B. Wu, X. Guo, Y. Jiang, W. Li, B. Guo, C. Ye, W. Su, J. Fang, X. Ou, F. Liu, Z. Wei, T. C. Sum. T. P. Russell and Y. Li, *Adv. Mater.*, 2018, **30**, 1704546

41   T. Liu, L. Huo, S. Chandrabose, K. Chen, G. Han, F. Qi, X. Meng, D. Xie, W. Ma, Y. Yi, J. M. Hodgkiss, F. Liu, J. Wang, C. Yang and Y. Sun, *Adv. Mater.*, 2018, **30**, 1707353.

42   L. Ye, Y. Xie, K, Weng, H. S. Ryu, C. Li, Y. Cai, H. Fu, D. Wei, H. Y. Woo, S. Tan and Y. Sun, *Nano Energy,* 2019, **58**, 220-226.

43   P. Chao, L. Liu, J. Zhou, J. Qu, D. Mo, H. Meng, Z. Xie, F. He and Y. Ma, *ACS Appl. Energy Mater.*, 2018, **1**, 6549-6559.

44   A. Tang, W. Song, B. Xiao, J. Guo, J. Min, Z. Ge, J. Zhang, Z. Wei and E. Zhou, *Chem. Mater.*, 2019, **31**, 3941-3947.

45   W. Zhao, S. Li, H. Yao, S. Zhang, Y. Zhang, B. Yang and J. Hou, *J. Am. Chem. Soc.,* 2017, **139**, 7148-7151.

46   F. Zhao, D. He, J. Xin, S. Dai, H. Xue, L. Jiang, Z. Wei, W. Ma, X. Zhan, Y. Li and C. Wang, *Sci. China Chem.*, 2019, **62**, 790-796.

47   D. Meng, D. Sun, C. Zhong, T. Liu, B. Fan, L. Huo, Y. Li,W. Jiang, H. Choi, T. Kim, J. Y. Kim, Y. Sun, Z. Wang and A. J. Heeger, *J. Am. Chem. Soc.*, 2016, **138**, 375-380.

48   T. Li, S. Dai, Z. Ke, L. Yang, J. Wang, C. Yan, W. Ma and X. Zhan, *Adv. Mater.*, 2018, **30**, 1705969.

49   P. W. M. Blom, V. D. Mihailetchi, L. J. A. Koster and D. E. Markov, *Adv. Mater.*, 2007, **19**, 1551-1566.

50   A. K. K. Kyaw, D. H. Wang, V. Gupta, W. L. Leong, L. Ke, G. C. Bazan and A. J. Heeger, *ACS Nano*, 2013, **7**, 4569-4577.

51   L.J. Koster, V. D. Mihailetchi, R. Ramaker and P. W. M. Blom, *Appl.Phys. Lett.,* 2005, **86**, 123509.

52 R. Steyrleuthner, R. D. Pietro, Brian. A. Collins, F. Polzer, S. Himmelberger, M. Schubert, Z. Chen, S. Zhang, A. Salleo, H. Ade, A. Facchetti and D. Neher, *J. Am. Chem. Soc.*, 2014, **136**, 4245-4256.

53 M. Schubert, B. A. Collins, H. Mangold, I. A. Howard, W. Schindler, K. Vandewal, S. Roland, J. Behrends, F. Kraffert, R. Steyrleuthner, Z. Chen, K. Fostiropoulos, R. Bittl, A. Salleo, A. Facchetti, F. Laquai, H. Ade and D. Neher, *Adv. Funct. Mater.*, 2014, **24**, 4068-4081.

54 T. Xia, Y. Cai, H. Fu and Y. Sun, *Sci. China Chem.*, 2019, **62**, 662-668.

55 K. H. Hendriks, G. H. Heintges, V. S. Gevaerts, M. M. Wienk and R. A. Janssen, *Angew. Chem. Int. Ed.*, 2013, **52**, 8341-8344.

56 J. Lee, S. B. Jo, M. Kim, H. G. Kim, J. Shin, H. Kim and K. Cho, *Adv. Mater.*, 2014, **26**, 6706-6714.

57 S. Zhang, Y. Qin, J. Zhu and J. Hou, Adv. Mater. 2018, **30**, 1800868

58 M. J. Frisch, G. W. Trucks, H. B. Schlegel, G. E. Scuseria, M. A. Robb, J. R. Cheeseman, G. Scalmani, V. Barone, G. A. Petersson, H. Nakatsuji, X. Li, M. Caricato, A. V. Marenich, J. Bloino, B. G. Janesko, R. Gomperts, B. Mennucci, H. P. Hratchian, J. V. Ortiz, A. F. Izmaylov, J. L. Sonnenberg, D. Williams-Young, F. Ding, F. Lipparini, F. Egidi, J. Goings, B. Peng, A. Petrone, T. Henderson, D. Ranasinghe, V. G. Zakrzewski, J. Gao, N. Rega, G. Zheng, W. Liang, M. Hada, M. Ehara, K. Toyota, R. Fukuda, J. Hasegawa, M. Ishida, T. Nakajima, Y. Honda, O. Kitao, H. Nakai, T. Vreven, K. Throssell, J. A. Montgomery, J. Jr., E. Peralta, F. Ogliaro, M. J. Bearpark, J. J. Heyd, E. N. Brothers, K. N. Kudin, V. N. Staroverov, T. A. Keith, R. Kobayashi, J. Normand, K. Raghavachari, A. P. Rendell, J. C. Burant, S. S. Iyengar, J. Tomasi, M. Cossi, J. M. Millam, M. Klene, C. Adamo, R. Cammi, J. W. Ochterski, R. L. Martin, K. Morokuma, O. Farkas, J. B. Foresman and D. J. Fox, Gauussian 16, Gaussian, Inc.: Wallingford, CT, 2016.

ToC Figure